Modulation of Energetic Electron Precipitation Driven by Three Types of Whistler Mode Waves

Xiao-Chen Shen[1], Wen Li[1], Luisa Capannolo[1], Qianli Ma[1,2], Murong Qin[1,3], Anton V. Artemyev[4], Vassilis Angelopoulos[4], Xiao-Jia Zhang[4, 5], and Sheng Huang[1]

[1] Center for Space Physics, Boston University, Boston, MA, USA.

[2] Department of Atmospheric and Oceanic Sciences, University of California, Los Angeles, CA, USA.

[3] Cooperative Programs for the Advancement of Earth System Science, UCAR, Boulder, Colorado, USA.

[4] Department of Earth, Planetary, and Space Sciences, University of California, Los Angeles, CA, USA

[5]Department of Physics, University of Texas at Dallas, Richardson, USA

Corresponding authors:

Xiao-Chen Shen (sdusxc@gmail.com)

Wen Li (luckymoon761@gmail.com)

Key Points:

- Modulated electron precipitation from tens to hundreds of keV over *L* shells of 4-9 is observed by ELFIN at low altitudes
- A good correlation is observed between the spatial variations of electron precipitation and wave intensities of hiss, plume hiss, and chorus
- Quasi-linear modeling based on the observed wave and plasma parameters reproduced the observed electron precipitation

Abstract

Precipitation into the Earth's atmosphere due to pitch angle scattering by plasma waves has been recognized as one of the major loss mechanisms for energetic electrons. In this study, we quantitatively evaluate their roles in precipitating electrons during a conjunction event with modulated electron precipitation observed at low altitudes by Electron Loss and Fields INvestigation (ELFIN) and three types of whistler mode waves (hiss, plume hiss, and chorus) measured near the equator by Time History of Events and Macroscale Interactions during Substorms (THEMIS). Electron precipitation was observed from~50 keV to <1 MeV with a spatial modulation, suggested by a good correlation between L shell-sorted precipitation fluxes and wave intensities. A quasi-linear analysis supports the observed energy range of precipitation and the ratio of precipitating-to-trapped flux. Our findings reveal that the modulated energetic electron precipitation is driven by hiss, plume hiss, and chorus waves.

Plain Language Summary

Energetic electrons precipitated from the inner magnetosphere into the upper atmosphere can form diffuse and discrete aurora and modulate the ionospheric conductance. One of the major drivers of electron precipitation is wave-particle interaction with whistler mode waves. In this study, we use the ELFIN CubeSats to measure electron precipitation at low altitudes and the THEMIS to provide wave and plasma measurements near the magnetic equator in the conjugate locations. We find that the electron precipitation rate is highly correlated to the whistler mode wave intensity near the equator. Through a quasi-linear analysis, we demonstrate that the modulation of electron precipitation is driven by whistler mode hiss, plume hiss, and chorus waves that occur in an extensive region of the Earth's magnetosphere.

1 Introduction

Whistler mode waves are right-hand polarized electromagnetic waves with frequencies below electron cyclotron frequency (e.g., Stix, 1992). Multiple types of whistler mode waves are observed inside the Earth's magnetosphere, including plasmaspheric hiss, plume hiss, and chorus waves (e.g., Chan & Holzer, 1976; Horita, 1977; W. Li et al., 2019; Meredith et al., 2018; Nakamura et al., 2018; Summers et al., 2007; Thorne et al., 1974). Among them, plasmaspheric hiss (hiss for short) is typically incoherent with a broadband frequency structure typically from 20 to 2,000 Hz, and is observed inside the plasmasphere with a peak intensity near L ~3 on the dayside (e.g., W. Li et al., 2015; Meredith et al., 2013; S. Zhang et al., 2021). Plume hiss, as indicated by its name, is hiss wave in plasmaspheric plume regions extending to higher L shells (e.g., Shi et al., 2019; W. Zhang et al., 2019). Chorus wave is a coherent whistler mode wave with a frequency chirping feature that is mainly observed in low density trough regions with stronger intensities in the midnight-dawn-noon sectors (e.g., W. Li et al., 2011, 2013; Meredith et al., 2012, 2020, 2021; Ni et al., 2014; Shen et al., 2019).

Extensive studies have demonstrated that these three types of whistler mode waves can efficiently drive electron precipitation from the Earth's inner magnetosphere into the upper atmosphere due to pitch angle diffusion through cyclotron and Landau resonant interactions with energetic electrons (e.g., Kataoka et al., 2020; W. Li et al., 2019; Ma et al., 2020, 2021; Miyoshi et al., 2015, 2021; Nishimura et al., 2010; Ozaki et al., 2019). Due to their similar frequency range inside the Earth's magnetosphere, they interact with energetic electrons with energies ranging from several to hundreds of keV. During disturbed geomagnetic conditions (AE > 500

nT), chorus waves drive 3-10 erg/cm^2/s electron precipitation predominantly in the pre-dawn sector at $L > 4$, while hiss and plume hiss drive 0.3-1 erg/cm^2/s electron precipitation at lower L shells (Ma et al., 2020, 2021). Based on both an event analysis and a statistical study, plume hiss is suggested to be more efficient in driving electron precipitation than plasmaspheric hiss (W. Li et al., 2019; Ma et al., 2021).

Modulated electron precipitation on ultra-low frequency (ULF) scales has been reported by several studies with a period in the Pc4 or Pc5 frequency range (e.g., Brito et al., 2012; Jaynes et al., 2015; Manninen et al., 2010; Motoba et al., 2013; Qin et al., 2021; Rae et al., 2007, 2018; Spanswick et al., 2005; Xia et al., 2016; X. Zhang et al., 2019). During these reported events, ULF oscillations modulated whistler mode wave amplitude and/or the size of the bounce loss cone and hence modulated the electron precipitation rates. On a longer timescale, the so-called 'breathing mode', due to the solar wind buffeting of the magnetosphere, can also produce modulated electron precipitation (e.g., Breneman et al., 2015).

However, the observed precipitation modulation cannot always be explained by temporal variations due to ULF waves or solar wind variations. Furthermore, prior to the launch of Electron Loss and Fields INvestigation (ELFIN), electron measurements at low altitudes typically did not provide full pitch angle coverage with sufficient energy resolution to distinguish precipitating electrons from trapped electrons without ambiguity. In this study, we take advantage of the conjugate observation of electron distribution at low altitudes by ELFIN and wave and plasma distributions near the equator by Time History of Events and Macroscale Interactions during Substorms (THEMIS) to reveal the drivers of the modulated energetic electron precipitation.

2 Modulated Electron Precipitation at Low Altitudes

We use low-altitude observations from the ELFIN CubeSats to provide measurements of precipitating and mirroring energetic electrons over a broad L shell range (Angelopoulos et al., 2020). ELFIN is a dual-probe CubeSat mission launched on September 15, 2018, orbiting at an altitude of ~450 km with an orbital period of ~1.5 hours. Each probe is equipped with an Energetic Particle Detector (EPD) that measures electrons from ~50 keV to 6 MeV with full pitch angle coverage. The time resolution of ELFIN EPD data is ~0.14 s. In a full spin period (~3 s), there are ~20 electron measurements with varying looking directions. In this study, we binned the data into each 3-second time window in 18 pitch angle sectors covering from 0 to 180 degrees.

Figure 1 presents the ELFIN measurements of electron distributions as well as the solar wind and geomagnetic conditions during an interesting event, which occurred from 14:21 to 14:24 UT on November 27, 2020. The solar wind dynamic pressure remained relatively steady in the range of 1.5-2.5 nPa over five hours prior to the observed precipitation event (Figure 1a). The interplanetary magnetic field (IMF) was mostly southward until an hour before the event (Figure 1a), which is preferential for substorm activity when electrons are injected towards Earth. The Sym-H index, an indicator of the ring current strength, ranged from -24 to -8 nT, which was not intense (Figure 1b). The AE index was continuously above 300 nT with the peak value reaching ~800 nT during the preceding five hours, indicating on-going substorm activity (Figure 1b). ELFIN-A observed modulated trapped and precipitating energetic electron flux in this event within three minutes covering L shells from 4 to 9 on the dayside at magnetic local time (MLT) ~

11 hr (Figures 1c and 1d). The trapped electron flux was high (~60 keV to < 1 MeV at $L > 6$, and up to 3 MeV at $L < 6$), while the precipitating electrons were mainly below 1 MeV. The ratio of precipitating-to-trapped electrons was approaching one at tens to hundreds of keV, indicative of almost full loss cone, but remained < 0.1 at higher energies (Figure 1e). Electron pitch angle distributions (Figures 1f–1i) exhibited asymmetric distributions with higher electron flux within the loss cone (black solid lines) than that within the anti-loss cone (black dashed lines) at various energy channels. However, electron precipitation at > 1 MeV was not intense and mostly occurred near the edge of the bounce loss cone (Figure 1i).

We suggest that the observed electron precipitation at tens to hundreds of keV energies is related to pitch angle scattering by whistler mode waves, instead of electromagnetic ion cyclotron (EMIC) waves, which typically account for electron precipitation at energies above several hundreds of keV (e.g., Blum et al., 2015; Capannolo, Li, Ma, Shen, et al., 2019; Capannolo, Li, Ma, Chen, et al., 2019; Jordanova et al., 2008; Z. Li et al., 2014; Miyoshi et al., 2008; Qin et al., 2018; X.-J. Zhang et al., 2021).

3 Conjugate Observations of Plasma Waves near the Equator

To identify the driver of modulated energetic electron precipitation and determine whether the observed modulation is spatial or temporal, we use plasma and wave measurements from the electrostatic analyzer (ESA), solid state telescope (SST), search coil magnetometer (SCM) and fluxgate magnetometer (FGM) instruments onboard one of the five THEMIS probes (Angelopoulos, 2008; Auster et al., 2008; McFadden et al., 2008; Roux et al., 2008), which was orbiting near the magnetic equator and had two tight conjunctions with ELFIN-A and ELFIN-B (see Figure S2 in Supporting Information for ELFIN-B observations) near ~ 1423 and 1545 UT, respectively (Figures 2a and 2b). During the two tight conjunctions, the separation between the two probes is less than 1.5 hours in MLT. THEMIS-E took three hours (~1400 to 1700 UT) to travel through L shells from 4 to 9, which is much longer than the ~3 minutes used by ELFIN at low altitudes. Based on the total electron density inferred from the spacecraft potential, one can see that THEMIS-E was traveling from the plasmasphere to plasmaspheric plume regions near L~ 6 and then entered the plasma trough region at higher L shells (Figure 2c). Measurements of wave magnetic and electric fields indicate the intensification of hiss, plume hiss, and chorus waves in the three different regions, respectively (Figures 2d and 2e). The magnetic field data from SCM on THEMIS-E are still pending calibration beyond 2017, although the relative intensity showing wave activities is not affected (Tsai et al., 2022; X.-J. Zhang et al., 2022). Measurements of magnetic spectral density from the Plasma Wave Experiment (PWE) onboard Arase (Kasahara et al., 2018) during a conjunction period within this day (see Figure S1 in the supporting information for detailed information) were used to calibrate the magnetic spectral density values from THEMIS-E (e.g., Dudok de Wit et al., 2022; Santolík et al., 2021). The magnetic spectral density was scaled up by a factor of 2 to match the observations from Arase during the conjunction. Hiss and plume hiss were intense with wave amplitudes reaching ~ 100-200 pT, while chorus waves were not strong (10 to 20 pT) (Figure 2f). These observations show the plasma wave activity near the equatorial plane in the L shell range of 4 to 9, which is the region where modulated electron precipitation was observed by ELFIN. Whistler mode waves, including hiss, plume hiss, and chorus waves, with modulating amplitudes together with varying plasma conditions at different L shells, may contribute to the observed modulated electron precipitation. From ~16:00 UT to 18:30 UT (at $L > 7.5$), H^+ band EMIC wave activities were

158 also observed by THEMIS-E with wave magnetic amplitudes, integrated over frequencies from
159 the helium gyrofrequency to the hydrogen gyrofrequency, less than 0.2 nT (not shown).

160 **4 Quantification of Electron Precipitation Using Quasi-Linear Theory**

161 In order to estimate the ratio of precipitating-to-trapped electron fluxes due to wave-particle
162 interactions, we apply the UCLA Full Diffusion Code (Ma et al., 2020, 2021; Ni et al., 2008,
163 2011) based on quasi-linear theory to compute the diffusion coefficients. We use wave spectra
164 and surrounding plasma parameters, including total electron density and magnetic field
165 magnitude, at three time snapshots (14:19 UT, 14:48 UT, and 15:45 UT, see orange dashed lines
166 in Figure 2) for hiss, plume hiss, and chorus waves, respectively. Survey mode plasma wave
167 measurements from THEMIS-E do not provide the wave normal angle (WNA) and the burst
168 mode was not operating during this event. Thus, we assume a gaussian distribution of WNA with
169 the peak WNA to be parallel to the magnetic field line and a WNA width of 30º (Hartley et al.,
170 2018; W. Li et al., 2011; Santolík et al., 2014; Taubenschuss et al., 2014). Resonant harmonic
171 numbers from -10 to 10 and magnetic latitudes within 50 degrees are used in the calculation
172 including effects from both cyclotron and Landau resonances.

173 The calculated bounce-averaged electron pitch angle diffusion rates are shown in Figures 3a–3c.
174 Parameters including L shell, background magnetic field magnitude, the ratio of plasma to
175 electron gyro frequency, and wave amplitude, used to calculate the pitch angle diffusion rates,
176 are included in Table S1 in the supporting information. For the three wave modes, the energies of
177 electrons subject to efficient scattering are in the range of several keV to hundreds of keV.
178 Landau resonance occurred at low energies or near pitch angles close to 90º. In this study, we
179 focus on the diffusion rates near the loss cone indicated by the magenta dashed lines to evaluate
180 electron precipitation. Among the three waves, chorus waves drive the least efficient pitch angle
181 scattering of electrons due to the low wave amplitude (19 pT). The hiss and plume hiss drive
182 more efficient pitch angle scattering given their large wave amplitudes (222 and 121 pT) at the
183 selected times.

184 The pitch angle diffusion rates at the loss cone and the strong diffusion limit (D_{SD}) for varying
185 energies are plotted in Figures 3d–f as red solid and dashed lines, respectively. The derived pitch
186 angle diffusion rate due to plume hiss is very close to the strong diffusion limit at tens to
187 hundreds of keV, although the diffusion rates due to all the three wave modes do not exceed the
188 strong diffusion limit. The diffusion rates decrease significantly at energies below 10 keV for
189 hiss and plume hiss waves but remain high down to ~4 keV for chorus waves since their upper
190 frequency limit is higher to interact with lower energy electrons. However, this difference cannot
191 be captured by ELFIN since electron measurements only extend down to ~60 keV.

192 Based on these diffusion rates near the loss cone, we calculate the loss cone filling index (Ni et
193 al., 2014), which is similar to the ratio of precipitating-to-trapped electrons from the ELFIN
194 observations, as following

195 $$\chi(E) = \frac{2\int_0^1 I_0[Z_0(E)\tau]\cdot\tau\cdot d\tau}{I_0[Z_0(E)]} \quad , \qquad (1)$$

where I_0 is the modified Bessel function of the first kind, $Z_0 = \sqrt{\frac{D_{SD}}{(<D_{\alpha\alpha}>|_{LC})}}$ is the square root of the ratio of strong diffusion limit and pitch angle diffusion rate at the loss cone at various energies, and τ is an integration variable. The calculated loss cone filling index is shown in Figures 3d–3f as green lines. The peak loss cone filling index is around tens of keV and drops to below 0.1 at 1 MeV for the three wave modes.

To better compare the observed and modeled electron precipitation, we binned observations from both THEMIS and ELFIN and the modeling results into *L*-shell bins of 0.05 width, from *L* = 4 to *L* = 9 (Figure 4). Note that the color bar in this plot represents the universal time (UT). Electron density and wave amplitude variations (Figures 4a and 4b) near the edge of the plasmasphere and plume regions become smoother and less distinct than those shown in Figure 2 due to binning. Within the blue and orange shaded areas (corresponding to the region where hiss and chorus waves were observed by THEMIS), THEMIS and ELFIN were located at a similar *L* shell and UT. Within the green shaded region, THEMIS and ELFIN were crossing a similar *L* shell, but with ~0.5 to 1 hr time difference. The observed electron precipitation at 100 keV shows a similar trend to the observed whistler mode wave amplitude variations, especially during the two tight conjunctions (Figure 4c). Figure 4d is the modeled loss cone filling index at 100 keV binned by *L* shell, and it well reproduced the observed ratio of precipitating-to-trapped electron flux by ELFIN-A. The hiss-driven precipitation leads to a ratio of precipitating-to-trapped electrons reaching 0.8 with two peak structures, while chorus waves, in this case, only drive electron precipitation with a ratio around 0.4. The modeled plume hiss-driven precipitation ratio is lower than the observed, which may be due to the UT difference in this case. THEMIS provided plume hiss measurements (~14:50 UT) ~30 minutes later than the ELFIN measurements of electron precipitation (~14:23 UT) during the recovery of a substorm, indicated by the AE index (Figure 1b). The underestimated electron precipitation reproduced based on the THEMIS measurements may be due to the decrease in plume hiss wave intensity or the narrowing of plumes due to the temporal evolution. However, the trend of precipitation ratio as a function of *L* shell is overall well reproduced. The peaks in *L* shell shift within 0.2 *L* are reasonable considering the uncertainties in the IGRF magnetic field models. At the higher energy of 500 keV (Figures 4e and 4f), the precipitation ratio becomes lower; it decreased to ~0.2 for hiss-driven precipitation and ~0.1 for chorus-driven precipitation. Due to the low counts of electrons at high energies (> 100s keV), the obtained precipitation ratio at 500 keV shown in Figure 4e becomes sparse at *L* > ~7 during this event. Nevertheless, the available measurements show remarkable agreement between the observations and modeling, especially in terms of the trend of precipitation ratio as a function of *L* shell.

5 Summary

In the present paper, we analyzed an intriguing event of modulated electron precipitation due to whistler mode hiss, plume hiss, and chorus waves. The modulation of low-altitude electron precipitation is highly correlated with spatial variations of whistler mode wave amplitudes of hiss, plume hiss and chorus waves in the plasmasphere, plume and plasma trough, respectively. Using quasi-linear modeling, the observed ratio of precipitating-to-trapped electrons is well reproduced. These three types of whistler mode waves overall drive electron precipitation with energies ranging from tens of keV to less than 1 MeV, while chorus waves drive electron precipitation at slightly lower energies because of the higher wave frequency. The reproduced

precipitation ratio (peaking at ~0.4) due to plume hiss is lower than the observed one (peaking at ~1), which is likely due to the ~0.5 hr difference in UT between THEMIS and ELFIN, and associated variability of hiss wave intensity. The plume region may become narrower as time goes on and the spatially averaged wave amplitude becomes smaller (Figure 4). However, the two-peak structure is well reproduced. Moreover, plume hiss within the plume regions can still produce a ratio of precipitating to trapped electrons close to 1 at 10s of keV, although they may become narrower spatially (Figures 3b and 3e). Therefore, the plume hiss can drive very efficient electron precipitation (Figure 3b), in agreement with previous studies (W. Li et al., 2019; Ma et al., 2021) showing the importance of plume hiss in driving electron precipitation compared to the other two whistler mode waves. Overall, the remarkable correlation between the ELFIN observations of electron precipitation, THEMIS observations of whistler mode wave amplitudes, and the modeled precipitation ratio suggests that the observed modulation of electron precipitation is likely a spatial variation in this event.

These results, obtained by combining observations and modeling, suggest that whistler mode waves, including hiss, plume hiss and chorus at various regions from plasmasphere, plume and trough, contribute together to modulated electron precipitation (tens to hundreds of keV) into the upper atmosphere in an extensive region of the coupled magnetosphere-ionosphere system. The spatial variation of their wave amplitude and ambient plasma conditions affects the efficiency of electron pitch angle scattering, which leads to the modulated energetic electron precipitation observed at low altitudes. Since plasmaspheric hiss, plume hiss, and chorus occur over a wide range of MLT sectors on the dayside, our findings imply that modulations of electron precipitation caused by the three types of whistler mode waves are likely common in the broad region of the dayside magnetosphere, particularly when a plume region exists.

Acknowledgments

XS, WL and QM would like to acknowledge the NASA grants 80NSSC19K0845, 80NSSC20K0698, 80NSSC20K0196, 80NSSC21K1312, NSF grants AGS-2019950 and AGS-1847818, and the Alfred P. Sloan Research Fellowship FG-2018-10936. The UCLA team acknowledges NASA awards 80NSSC22K1005 and NAS5-02099 and NSF grant AGS-2019950. We acknowledge the ELFIN mission for providing electron measurements at low altitude. We also thank the following individuals for data from the THEMIS mission: J. W. Bonnell and F. S. Mozer for EFI data, O. LeContel for SCM data, and K. H. Glassmeier, U. Auster and W. Baumjohann for FGM data provided under the lead of the TU-BS and with financial support through the German Ministry for Economy and Technology and DLR under contract 50 OC 0302.

Open Research

Data from the THEMIS is publicly available at http://themis.ssl.berkeley.edu/data/themis. Data from the ELFIN is publicly available at https://data.elfin.ucla.edu/. Data from the Arase is publicly available at https://ergsc.isee.nagoya-u.ac.jp/. We use SPEDAS in IDL to process data files (Angelopoulos et al., 2019).

References

Angelopoulos, V. (2008). The THEMIS Mission. *Space Science Reviews*, *141*(1–4), 5–34. https://doi.org/10.1007/s11214-008-9336-1

Angelopoulos, V., Cruce, P., Drozdov, A., Grimes, E. W., Hatzigeorgiu, N., King, D. A., Larson, D., Lewis, J. W., McTiernan, J. M., Roberts, D. A., Russell, C. L., Hori, T., Kasahara, Y., Kumamoto, A., Matsuoka, A., Miyashita, Y., Miyoshi, Y., Shinohara, I., Teramoto, M., … Schroeder, P. (2019). The Space Physics Environment Data Analysis System (SPEDAS). *Space Science Reviews*, *215*(1), 9. https://doi.org/10.1007/s11214-018-0576-4

Angelopoulos, V., Tsai, E., Bingley, L., Shaffer, C., Turner, D. L., Runov, A., Li, W., Liu, J., Artemyev, A. V., Zhang, X.-J., Strangeway, R. J., Wirz, R. E., Shprits, Y. Y., Sergeev, V. A., Caron, R. P., Chung, M., Cruce, P., Greer, W., Grimes, E., … Zhang, G. Y. (2020). The ELFIN Mission. *Space Science Reviews*, *216*(5), 103. https://doi.org/10.1007/s11214-020-00721-7

Auster, H. U., Glassmeier, K. H., Magnes, W., Aydogar, O., Baumjohann, W., Constantinescu, D., Fischer, D., Fornacon, K. H., Georgescu, E., Harvey, P., Hillenmaier, O., Kroth, R., Ludlam, M., Narita, Y., Nakamura, R., Okrafka, K., Plaschke, F., Richter, I., Schwarzl, H., … Wiedemann, M. (2008). The THEMIS Fluxgate Magnetometer. *Space Science Reviews*, *141*(1–4), 235–264. https://doi.org/10.1007/s11214-008-9365-9

Blum, L. W., Halford, A., Millan, R., Bonnell, J. W., Goldstein, J., Usanova, M., Engebretson, M., Ohnsted, M., Reeves, G., Singer, H., Clilverd, M., & Li, X. (2015). Observations of coincident EMIC wave activity and duskside energetic electron precipitation on 18-19 January 2013: EMIC Waves and Electron Precipitation. *Geophysical Research Letters*, *42*(14), 5727–5735. https://doi.org/10.1002/2015GL065245

Breneman, A. W., Halford, A., Millan, R., McCarthy, M., Fennell, J., Sample, J., Woodger, L., Hospodarsky, G., Wygant, J. R., Cattell, C. A., Goldstein, J., Malaspina, D., & Kletzing, C. A. (2015). Global-scale coherence modulation of radiation-belt electron loss from plasmaspheric hiss. *Nature*, *523*(7559), 193–195. https://doi.org/10.1038/nature14515

Brito, T., Woodger, L., Hudson, M., & Millan, R. (2012). Energetic radiation belt electron precipitation showing ULF modulation: ULF WAVES AND RADIATION BELTS. *Geophysical Research Letters*, *39*(22). https://doi.org/10.1029/2012GL053790

Capannolo, L., Li, W., Ma, Q., Chen, L., Shen, X. -C., Spence, H. E., Sample, J., Johnson, A., Shumko, M., Klumpar, D. M., & Redmon, R. J. (2019). Direct Observation of Subrelativistic Electron Precipitation Potentially Driven by EMIC Waves. *Geophysical Research Letters*, *46*(22), 12711–12721. https://doi.org/10.1029/2019GL084202

Capannolo, L., Li, W., Ma, Q., Shen, X. -C., Zhang, X. -J., Redmon, R. J., Rodriguez, J. V., Engebretson, M. J., Kletzing, C. A., Kurth, W. S., Hospodarsky, G. B., Spence, H. E., Reeves, G. D., & Raita, T. (2019). Energetic Electron Precipitation: Multievent Analysis of Its Spatial Extent During EMIC Wave Activity. *Journal of Geophysical Research: Space Physics*, *124*(4), 2466–2483. https://doi.org/10.1029/2018JA026291

Chan, K.-W., & Holzer, R. E. (1976). ELF hiss associated with plasma density enhancements in the outer magnetosphere. *Journal of Geophysical Research*, *81*(13), 2267–2274. https://doi.org/10.1029/JA081i013p02267

Dudok de Wit, T., Krasnoselskikh, V. V., Agapitov, O., Froment, C., Larosa, A., Bale, S. D., Bowen, T., Goetz, K., Harvey, P., Jannet, G., Kretzschmar, M., MacDowall, R. J., Malaspina, D., Martin, P., Page, B., Pulupa, M., & Revillet, C. (2022). First Results From the SCM Search-Coil Magnetometer on Parker Solar Probe. *Journal of Geophysical Research: Space Physics*, *127*(4), e2021JA030018. https://doi.org/10.1029/2021JA030018

Hartley, D. P., Kletzing, C. A., Santolík, O., Chen, L., & Horne, R. B. (2018). Statistical Properties of Plasmaspheric Hiss From Van Allen Probes Observations. *Journal of Geophysical Research: Space Physics*, *123*(4), 2605–2619. https://doi.org/10.1002/2017JA024593

Horita, R. E. (1977). The source regions of fine structure in whistlers, auroral hiss and ELF hiss. *Journal of Atmospheric and Terrestrial Physics*, *39*(7), 793–798. https://doi.org/10.1016/0021-9169(77)90141-6

Jaynes, A. N., Lessard, M. R., Takahashi, K., Ali, A. F., Malaspina, D. M., Michell, R. G., Spanswick, E. L., Baker, D. N., Blake, J. B., Cully, C., Donovan, E. F., Kletzing, C. A., Reeves, G. D., Samara, M., Spence, H. E., & Wygant, J. R. (2015). Correlated Pc4–5 ULF waves, whistler-mode chorus, and pulsating aurora observed by the Van Allen Probes and ground-based systems. *Journal of Geophysical Research: Space Physics*, *120*(10), 8749–8761. https://doi.org/10.1002/2015JA021380

Jordanova, V. K., Albert, J., & Miyoshi, Y. (2008). Relativistic electron precipitation by EMIC waves from self-consistent global simulations: EMIC WAVES AND RELATIVISTIC ELECTRONS. *Journal of Geophysical Research: Space Physics*, *113*(A3). https://doi.org/10.1029/2008JA013239

Kasahara, Y., Kasaba, Y., Kojima, H., Yagitani, S., Ishisaka, K., Kumamoto, A., Tsuchiya, F., Ozaki, M., Matsuda, S., Imachi, T., Miyoshi, Y., Hikishima, M., Katoh, Y., Ota, M., Shoji, M., Matsuoka, A., & Shinohara, I. (2018). The Plasma Wave Experiment (PWE) on board the Arase (ERG) satellite. *Earth, Planets and Space*, *70*(1), 86. https://doi.org/10.1186/s40623-018-0842-4

Kataoka, R., Asaoka, Y., Torii, S., Nakahira, S., Ueno, H., Miyake, S., Miyoshi, Y., Kurita, S., Shoji, M., Kasahara, Y., Ozaki, M., Matsuda, S., Matsuoka, A., Kasaba, Y., Shinohara, I., Hosokawa, K., Uchida, H. A., Murase, K., & Tanaka, Y. (2020). Plasma Waves Causing Relativistic Electron Precipitation Events at International Space Station: Lessons From Conjunction Observations With Arase Satellite. *Journal of Geophysical Research: Space Physics*, *125*(9), e2020JA027875. https://doi.org/10.1029/2020JA027875

Li, W., Bortnik, J., Thorne, R. M., & Angelopoulos, V. (2011). Global distribution of wave amplitudes and wave normal angles of chorus waves using THEMIS wave observations. *Journal of Geophysical Research: Space Physics*, *116*, A12205. https://doi.org/10.1029/2011JA017035

Li, W., Ma, Q., Thorne, R. M., Bortnik, J., Kletzing, C. A., Kurth, W. S., Hospodarsky, G. B., & Nishimura, Y. (2015). Statistical properties of plasmaspheric hiss derived from Van Allen

Probes data and their effects on radiation belt electron dynamics. *Journal of Geophysical Research: Space Physics*, *120*(5), 3393–3405. https://doi.org/10.1002/2015JA021048

Li, W., Ni, B., Thorne, R. M., Bortnik, J., Green, J. C., Kletzing, C. A., Kurth, W. S., & Hospodarsky, G. B. (2013). Constructing the global distribution of chorus wave intensity using measurements of electrons by the POES satellites and waves by the Van Allen Probes: GLOBAL DISTRIBUTION OF CHORUS WAVES. *Geophysical Research Letters*, *40*(17), 4526–4532. https://doi.org/10.1002/grl.50920

Li, W., Shen, X.-C., Ma, Q., Capannolo, L., Shi, R., Redmon, R. J., Rodriguez, J. V., Reeves, G. D., Kletzing, C. A., Kurth, W. S., & Hospodarsky, G. B. (2019). Quantification of Energetic Electron Precipitation Driven by Plume Whistler Mode Waves, Plasmaspheric Hiss, and Exohiss. *Geophysical Research Letters*, *46*(7), 3615–3624. https://doi.org/10.1029/2019GL082095

Li, Z., Millan, R. M., Hudson, M. K., Woodger, L. A., Smith, D. M., Chen, Y., Friedel, R., Rodriguez, J. V., Engebretson, M. J., Goldstein, J., Fennell, J. F., & Spence, H. E. (2014). Investigation of EMIC wave scattering as the cause for the BARREL 17 January 2013 relativistic electron precipitation event: A quantitative comparison of simulation with observations. *Geophysical Research Letters*, *41*(24), 8722–8729. https://doi.org/10.1002/2014GL062273

Ma, Q., Connor, H. K., Zhang, X. -J., Li, W., Shen, X. -C., Gillespie, D., Kletzing, C. A., Kurth, W. S., Hospodarsky, G. B., Claudepierre, S. G., Reeves, G. D., & Spence, H. E. (2020). Global Survey of Plasma Sheet Electron Precipitation due to Whistler Mode Chorus Waves in Earth's Magnetosphere. *Geophysical Research Letters*, *47*(15). https://doi.org/10.1029/2020GL088798

Ma, Q., Li, W., Zhang, X.-J., Bortnik, J., Shen, X.-C., Connor, H. K., Boyd, A. J., Kurth, W. S., Hospodarsky, G. B., Claudepierre, S. G., Reeves, G. D., & Spence, H. E. (2021). Global Survey of Electron Precipitation due to Hiss Waves in the Earth's Plasmasphere and Plumes. *Journal of Geophysical Research: Space Physics*, *126*(8), e2021JA029644. https://doi.org/10.1029/2021JA029644

Manninen, J., Kleimenova, N. G., Kozyreva, O. V., & Turunen, T. (2010). Pc5 geomagnetic pulsations, pulsating particle precipitation, and VLF chorus: Case study on 24 November 2006: PC5, PULSATING ABSORPTION, AND VLF CHORUS. *Journal of Geophysical Research: Space Physics*, *115*(A8). https://doi.org/10.1029/2009JA014837

McFadden, J. P., Carlson, C. W., Larson, D., Ludlam, M., Abiad, R., Elliott, B., Turin, P., Marckwordt, M., & Angelopoulos, V. (2008). The THEMIS ESA Plasma Instrument and In-flight Calibration. *Space Science Reviews*, *141*(1–4), 277–302. https://doi.org/10.1007/s11214-008-9440-2

Meredith, N. P., Bortnik, J., Horne, R. B., Li, W., & Shen, X.-C. (2021). Statistical Investigation of the Frequency Dependence of the Chorus Source Mechanism of Plasmaspheric Hiss. *Geophysical Research Letters*, *48*(6). https://doi.org/10.1029/2021GL092725

Meredith, N. P., Horne, R. B., Bortnik, J., Thorne, R. M., Chen, L., Li, W., & Sicard-Piet, A. (2013). Global statistical evidence for chorus as the embryonic source of plasmaspheric hiss. *Geophysical Research Letters*, *40*(12), 2891–2896. https://doi.org/10.1002/grl.50593

Meredith, N. P., Horne, R. B., Kersten, T., Li, W., Bortnik, J., Sicard, A., & Yearby, K. H. (2018). Global Model of Plasmaspheric Hiss From Multiple Satellite Observations. *Journal of Geophysical Research: Space Physics*, *123*(6), 4526–4541. https://doi.org/10.1029/2018JA025226

Meredith, N. P., Horne, R. B., Shen, X.-C., Li, W., & Bortnik, J. (2020). Global Model of Whistler Mode Chorus in the Near-Equatorial Region ($|\lambda m| < 18°$). *Geophysical Research Letters*, *47*(11). https://doi.org/10.1029/2020GL087311

Meredith, N. P., Horne, R. B., Sicard-Piet, A., Boscher, D., Yearby, K. H., Li, W., & Thorne, R. M. (2012). Global model of lower band and upper band chorus from multiple satellite observations: GLOBAL MODEL OF WHISTLER MODE CHORUS. *Journal of Geophysical Research: Space Physics*, *117*(A10). https://doi.org/10.1029/2012JA017978

Miyoshi, Y., Hosokawa, K., Kurita, S., Oyama, S.-I., Ogawa, Y., Saito, S., Shinohara, I., Kero, A., Turunen, E., Verronen, P. T., Kasahara, S., Yokota, S., Mitani, T., Takashima, T., Higashio, N., Kasahara, Y., Matsuda, S., Tsuchiya, F., Kumamoto, A., … Nakamura, S. (2021). Penetration of MeV electrons into the mesosphere accompanying pulsating aurorae. *Scientific Reports*, *11*(1), Article 1. https://doi.org/10.1038/s41598-021-92611-3

Miyoshi, Y., Oyama, S., Saito, S., Kurita, S., Fujiwara, H., Kataoka, R., Ebihara, Y., Kletzing, C., Reeves, G., Santolik, O., Clilverd, M., Rodger, C. J., Turunen, E., & Tsuchiya, F. (2015). Energetic electron precipitation associated with pulsating aurora: EISCAT and Van Allen Probe observations: pulsating aurora. *Journal of Geophysical Research: Space Physics*, *120*(4), 2754–2766. https://doi.org/10.1002/2014JA020690

Miyoshi, Y., Sakaguchi, K., Shiokawa, K., Evans, D., Albert, J., Connors, M., & Jordanova, V. (2008). Precipitation of radiation belt electrons by EMIC waves, observed from ground and space. *Geophysical Research Letters*, *35*(23), L23101. https://doi.org/10.1029/2008GL035727

Motoba, T., Takahashi, K., Gjerloev, J., Ohtani, S., & Milling, D. K. (2013). The role of compressional Pc5 pulsations in modulating precipitation of energetic electrons: (PC5 MODULATION OF ELECTRON PRECIPITATION). *Journal of Geophysical Research: Space Physics*, *118*(12), 7728–7739. https://doi.org/10.1002/2013JA018912

Nakamura, S., Omura, Y., & Summers, D. (2018). Fine Structure of Whistler Mode Hiss in Plasmaspheric Plumes Observed by the Van Allen Probes. *Journal of Geophysical Research: Space Physics*, *123*(11), 9055–9064. https://doi.org/10.1029/2018JA025803

Ni, B., Li, W., Thorne, R. M., Bortnik, J., Green, J. C., Kletzing, C. A., Kurth, W. S., Hospodarsky, G. B., & de Soria-Santacruz Pich, M. (2014). A novel technique to construct the global distribution of whistler mode chorus wave intensity using low-altitude POES electron data: A novel technique for global wave model. *Journal of Geophysical Research: Space Physics*, *119*(7), 5685–5699. https://doi.org/10.1002/2014JA019935

Ni, B., Thorne, R., Liang, J., Angelopoulos, V., Cully, C., Li, W., Zhang, X., Hartinger, M., Le Contel, O., & Roux, A. (2011). Global distribution of electrostatic electron cyclotron harmonic waves observed on THEMIS: GLOBAL DISTRIBUTION OF ECH WAVES. *Geophysical Research Letters*, *38*(17). https://doi.org/10.1029/2011GL048793

Ni, B., Thorne, R. M., Shprits, Y. Y., & Bortnik, J. (2008). Resonant scattering of plasma sheet electrons by whistler-mode chorus: Contribution to diffuse auroral precipitation. *Geophysical Research Letters*, *35*(11), L11106. https://doi.org/10.1029/2008GL034032

Nishimura, Y., Bortnik, J., Li, W., Thorne, R. M., Lyons, L. R., Angelopoulos, V., Mende, S. B., Bonnell, J. W., Le Contel, O., Cully, C., Ergun, R., & Auster, U. (2010). Identifying the Driver of Pulsating Aurora. *Science*, *330*(6000), 81–84. https://doi.org/10.1126/science.1193186

Ozaki, M., Miyoshi, Y., Shiokawa, K., Hosokawa, K., Oyama, S., Kataoka, R., Ebihara, Y., Ogawa, Y., Kasahara, Y., Yagitani, S., Kasaba, Y., Kumamoto, A., Tsuchiya, F., Matsuda, S., Katoh, Y., Hikishima, M., Kurita, S., Otsuka, Y., Moore, R. C., … Shinohara, I. (2019). Visualization of rapid electron precipitation via chorus element wave–particle interactions. *Nature Communications*, *10*(1), 257. https://doi.org/10.1038/s41467-018-07996-z

Qin, M., Hudson, M., Millan, R., Woodger, L., & Shekhar, S. (2018). Statistical Investigation of the Efficiency of EMIC Waves in Precipitating Relativistic Electrons. *Journal of Geophysical Research: Space Physics*, *123*(8), 6223–6230. https://doi.org/10.1029/2018JA025419

Qin, M., Li, W., Ma, Q., Woodger, L., Millan, R., Shen, X.-C., & Capannolo, L. (2021). Multi-Point Observations of Modulated Whistler-Mode Waves and Energetic Electron Precipitation. *Journal of Geophysical Research: Space Physics*, *126*(12), e2021JA029505. https://doi.org/10.1029/2021JA029505

Rae, I. J., Mann, I. R., Dent, Z. C., Milling, D. K., Donovan, E. F., & Spanswick, E. (2007). Multiple field line resonances: Optical, magnetic and absorption signatures. *Planetary and Space Science*, *55*(6), 701–713. https://doi.org/10.1016/j.pss.2006.02.009

Rae, I. J., Murphy, K. R., Watt, C. E. J., Halford, A. J., Mann, I. R., Ozeke, L. G., Sibeck, D. G., Clilverd, M. A., Rodger, C. J., Degeling, A. W., Forsyth, C., & Singer, H. J. (2018). The Role of Localized Compressional Ultra-low Frequency Waves in Energetic Electron Precipitation. *Journal of Geophysical Research: Space Physics*, *123*(3), 1900–1914. https://doi.org/10.1002/2017JA024674

Roux, A., Le Contel, O., Coillot, C., Bouabdellah, A., de la Porte, B., Alison, D., Ruocco, S., & Vassal, M. C. (2008). The Search Coil Magnetometer for THEMIS. *Space Science Reviews*, *141*(1–4), 265–275. https://doi.org/10.1007/s11214-008-9455-8

Santolík, O., Macúšová, E., Kolmašová, I., Cornilleau-Wehrlin, N., & de Conchy, Y. (2014). Propagation of lower-band whistler-mode waves in the outer Van Allen belt: Systematic analysis of 11 years of multi-component data from the Cluster spacecraft. *Geophysical Research Letters*, *41*(8), 2729–2737. https://doi.org/10.1002/2014GL059815

Santolík, O., Miyoshi, Y., Kolmašová, I., Matsuda, S., Hospodarsky, G. B., Hartley, D. P., Kasahara, Y., Kojima, H., Matsuoka, A., Shinohara, I., Kurth, W. S., & Kletzing, C. A. (2021). Inter-Calibrated Measurements of Intense Whistlers by Arase and Van Allen Probes. *Journal of Geophysical Research: Space Physics*, *126*(9), e2021JA029700. https://doi.org/10.1029/2021JA029700

Shen, X., Li, W., Ma, Q., Agapitov, O., & Nishimura, Y. (2019). Statistical Analysis of Transverse Size of Lower Band Chorus Waves Using Simultaneous Multisatellite Observations. *Geophysical Research Letters*, *46*(11), 5725–5734. https://doi.org/10.1029/2019GL083118

Shi, R., Li, W., Ma, Q., Green, A., Kletzing, C. A., Kurth, W. S., Hospodarsky, G. B., Claudepierre, S. G., Spence, H. E., & Reeves, G. D. (2019). Properties of Whistler Mode Waves in Earth's Plasmasphere and Plumes. *Journal of Geophysical Research: Space Physics*, *124*(2), 1035–1051. https://doi.org/10.1029/2018JA026041

Spanswick, E., Donovan, E., & Baker, G. (2005). Pc5 modulation of high energy electron precipitation: Particle interaction regions and scattering efficiency. *Annales Geophysicae*, *23*(5), 1533–1542. https://doi.org/10.5194/angeo-23-1533-2005

Stix, T. H. (1992). *Waves in Plasmas*. Am. Inst. of Phys.

Summers, D., Ni, B., & Meredith, N. P. (2007). Timescales for radiation belt electron acceleration and loss due to resonant wave-particle interactions: 2. Evaluation for VLF chorus, ELF hiss, and electromagnetic ion cyclotron waves: RADIATION BELT ELECTRON TIMESCALES. *Journal of Geophysical Research: Space Physics*, *112*(A4). https://doi.org/10.1029/2006JA011993

Taubenschuss, U., Khotyaintsev, Y. V., Santolík, O., Vaivads, A., Cully, C. M., Contel, O. L., & Angelopoulos, V. (2014). Wave normal angles of whistler mode chorus rising and falling tones. *Journal of Geophysical Research: Space Physics*, *119*(12), 9567–9578. https://doi.org/10.1002/2014JA020575

Thorne, R. M., Smith, E. J., Fiske, K. J., & Church, S. R. (1974). Intensity variation of ELF hiss and chorus during isolated substorms. *Geophysical Research Letters*, *1*(5), 193–196. https://doi.org/10.1029/GL001i005p00193

Tsai, E., Artemyev, A., Zhang, X., & Angelopoulos, V. (2022). Relativistic electron precipitation driven by non-linear resonance with whistler-mode waves. *Journal of Geophysical Research: Space Physics*, e2022JA030338. https://doi.org/10.1029/2022JA030338

Xia, Z., Chen, L., Dai, L., Claudepierre, S. G., Chan, A. A., Soto-Chavez, A. R., & Reeves, G. D. (2016). Modulation of chorus intensity by ULF waves deep in the inner magnetosphere. *Geophysical Research Letters*, *43*(18), 9444–9452.

Zhang, S., Rae, I. J., Watt, C. E. J., Degeling, A. W., Tian, A., Shi, Q., Shen, X., Smith, A. W., & Wang, M. (2021). Determining the Temporal and Spatial Coherence of Plasmaspheric Hiss Waves in the Magnetosphere. *Journal of Geophysical Research: Space Physics*, *126*(2). https://doi.org/10.1029/2020JA028635

Zhang, W., Ni, B., Huang, H., Summers, D., Fu, S., Xiang, Z., Gu, X., Cao, X., Lou, Y., & Hua, M. (2019). Statistical Properties of Hiss in Plasmaspheric Plumes and Associated Scattering Losses of Radiation Belt Electrons. *Geophysical Research Letters*, *46*(11), 5670–5680. https://doi.org/10.1029/2018GL081863

Zhang, X., Chen, L., Artemyev, A. V., Angelopoulos, V., & Liu, X. (2019). Periodic Excitation of Chorus and ECH Waves Modulated by Ultralow Frequency Compressions. *Journal of Geophysical Research: Space Physics*, *124*(11), 8535–8550. https://doi.org/10.1029/2019JA027201

Zhang, X.-J., Artemyev, A., Angelopoulos, V., Tsai, E., Wilkins, C., Kasahara, S., Mourenas, D., Yokota, S., Keika, K., Hori, T., Miyoshi, Y., Shinohara, I., & Matsuoka, A. (2022). Superfast precipitation of energetic electrons in the radiation belts of the Earth. *Nature Communications*, *13*(1), 1611. https://doi.org/10.1038/s41467-022-29291-8

Zhang, X.-J., Mourenas, D., Shen, X.-C., Qin, M., Artemyev, A. V., Ma, Q., Li, W., Hudson, M. K., & Angelopoulos, V. (2021). Dependence of Relativistic Electron Precipitation in the Ionosphere on EMIC Wave Minimum Resonant Energy at the Conjugate Equator. *Journal of Geophysical Research: Space Physics*, *126*(5), e2021JA029193. https://doi.org/10.1029/2021JA029193

Figures and Captions

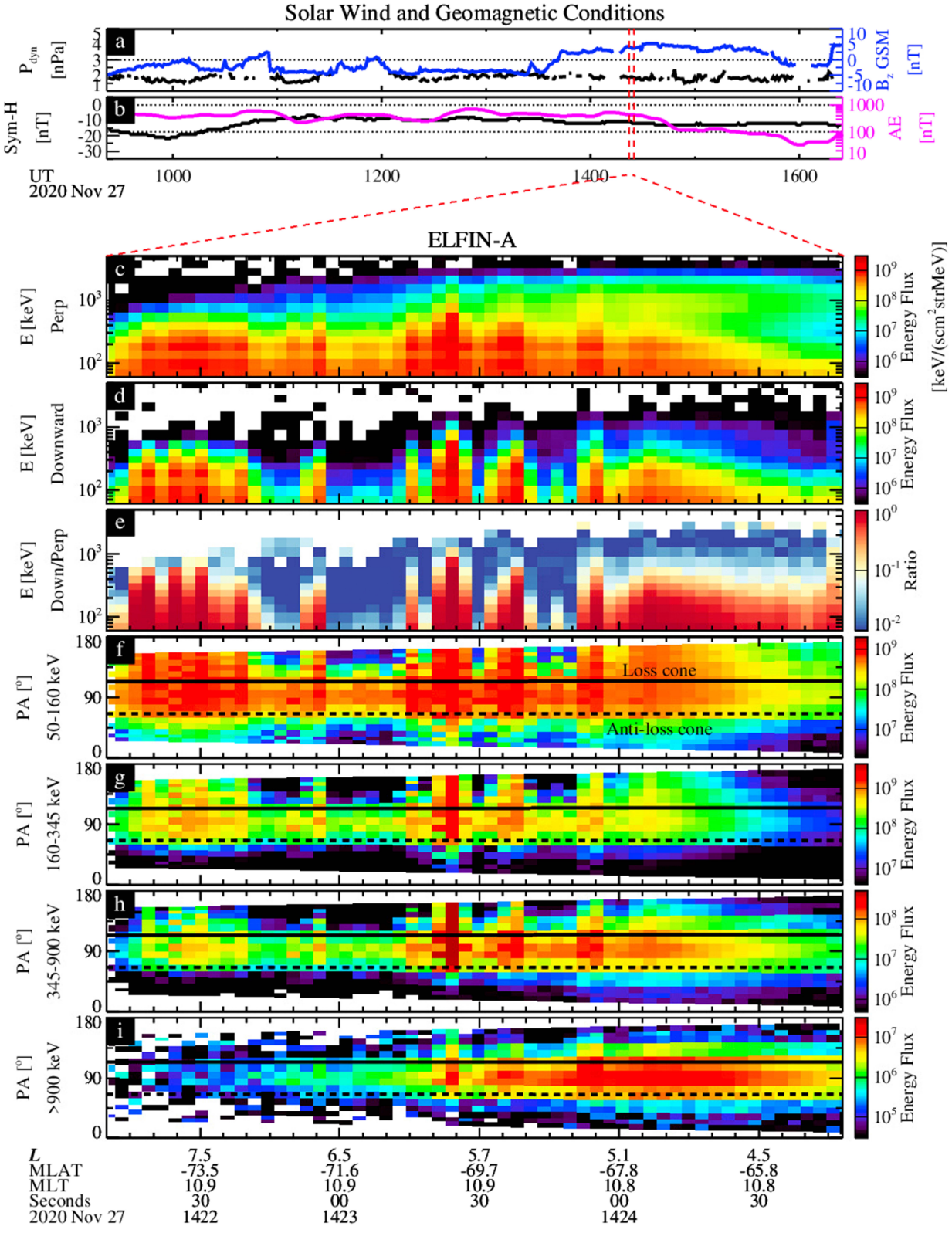

543 **Figure 1**. Solar wind, geomagnetic conditions, and ELFIN-A observations of precipitating and
544 trapped electrons at low Earth orbit. (a) Solar wind dynamic pressure (black) and interplanetary
545 magnetic field *z* component (blue) in GSM coordinates. (b) Geomagnetic Sym-H (black) and AE
546 indices (magenta). (c) Trapped electron energy flux spectrogram with local pitch angles near 90º.
547 (d) Precipitating electron energy flux spectrogram with pitch angles inside the bounce loss cone.
548 (e) Ratio of downward moving (precipitating) electrons to trapped electrons. (f–i) Pitch angle
549 distribution of electrons for energy channels of 50-160 keV, 160-345 keV, 345-900 keV, and >
550 0.9 MeV, respectively. Here the black solid (dashed) line represents loss cone (anti-loss cone).
551

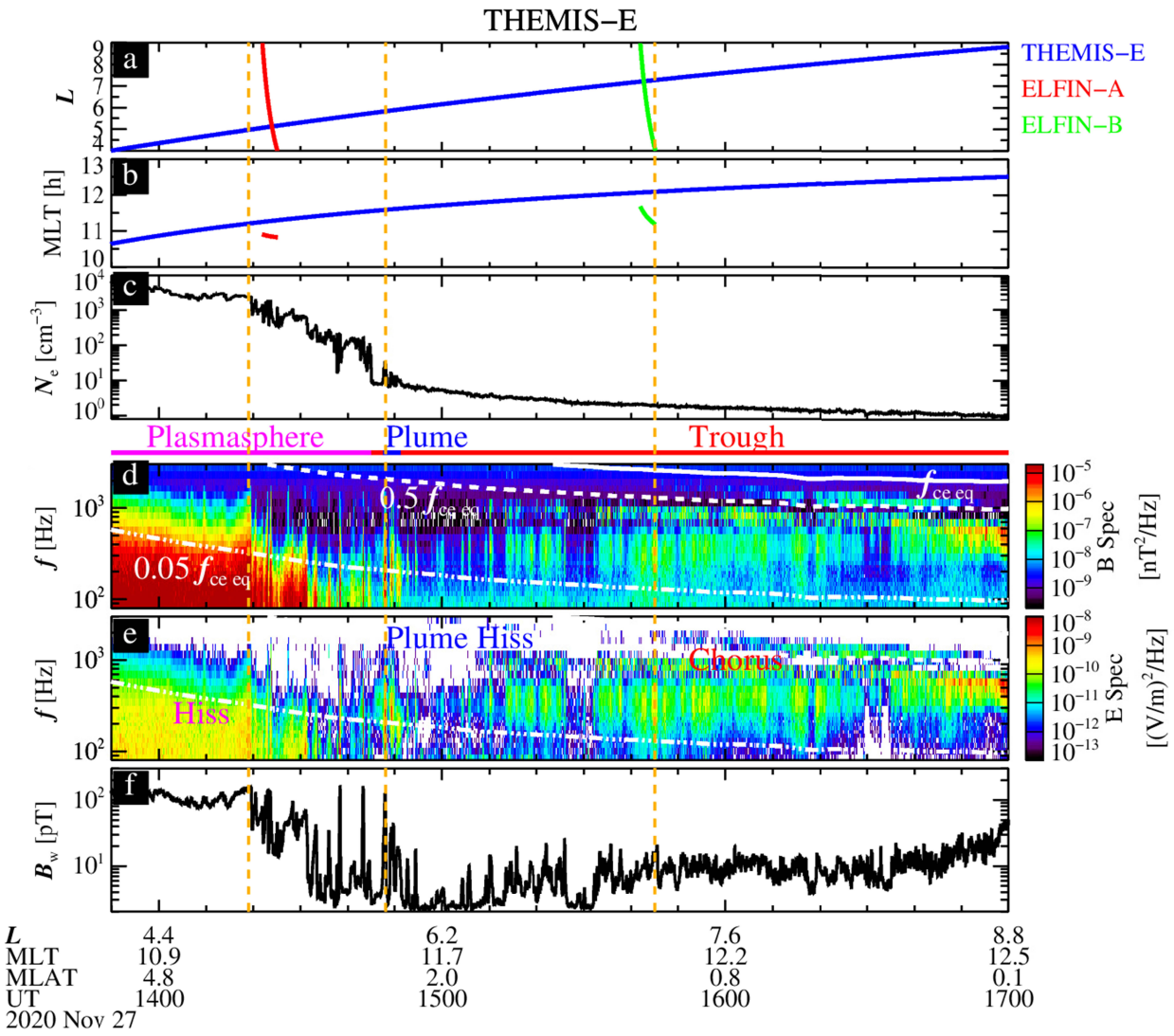

Figure 2. Conjugate observations near the magnetic equator from THEMIS-E. (a) *L* shell and (b) MLT for THEMIS-E (blue), ELFIN-A (red) and B (green) satellites. (c) Total electron density inferred from the spacecraft potential. (d) Wave magnetic and (e) electric spectral intensities, where the white solid, dashed and dash-dotted lines are equatorial electron gyrofrequency (f_{ce}), 0.5 f_{ce}, and 0.05 f_{ce}, respectively. (f) Whistler mode magnetic wave amplitude integrated from 80 Hz to the lower value of 2,000 Hz and f_{ce}. A horizontal bar between panels c and d illustrate different plasma regions, including plasmasphere (magenta), plume (blue), and plasma trough (red). Three orange dashed lines mark the time snapshots used to calculate pitch angle diffusion rates in Figure 3.

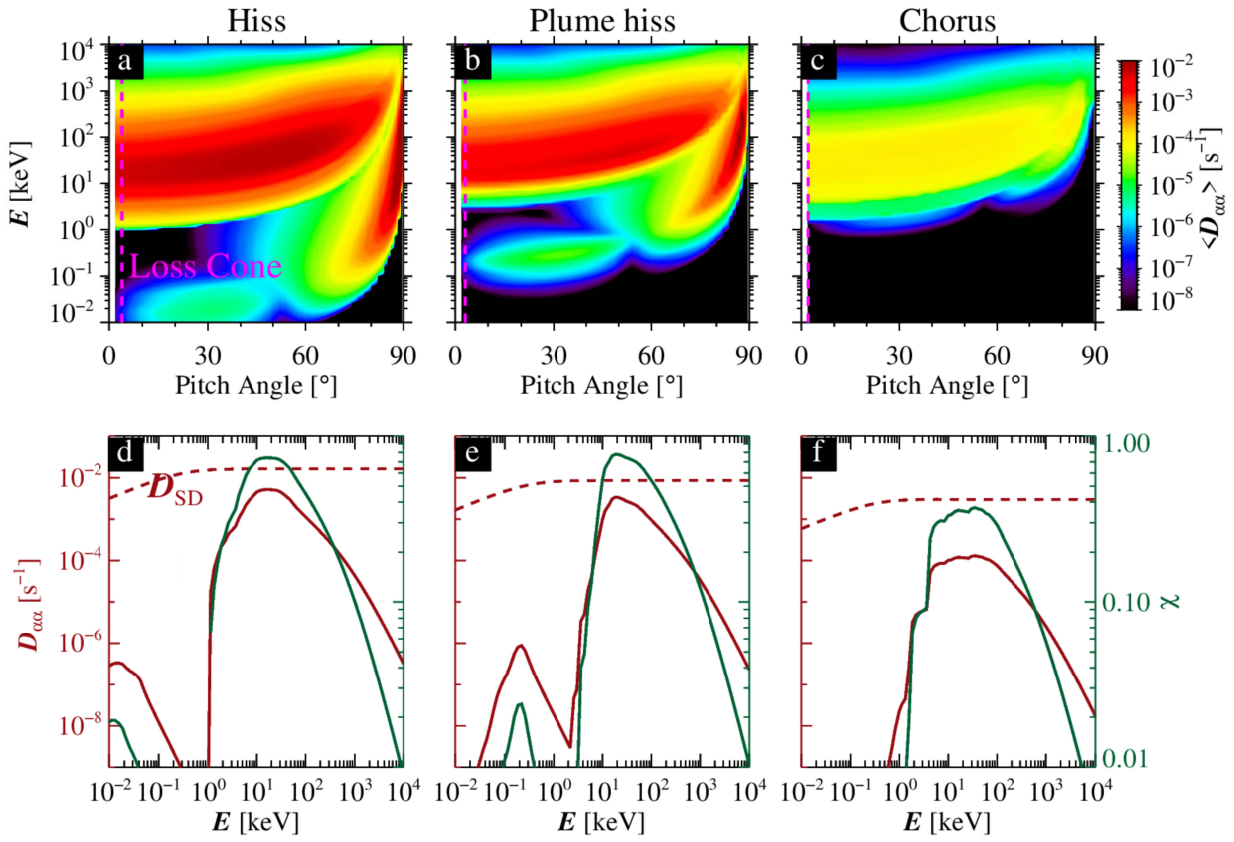

Figure 3. Effects of whistler mode waves on energetic electrons based on quasi-linear theory. (a) Pitch angle diffusion rates due to hiss waves, (b) plume hiss waves, and (c) chorus waves. (d) Pitch angle diffusion rates due to the observed hiss waves (red solid line), the strong diffusion rates (red dashed line) for electrons with pitch angles at the bounce loss cone, and the loss cone filling index (green line). (e–f) Similar to the panel (d) but for plume hiss and chorus waves, respectively.

571

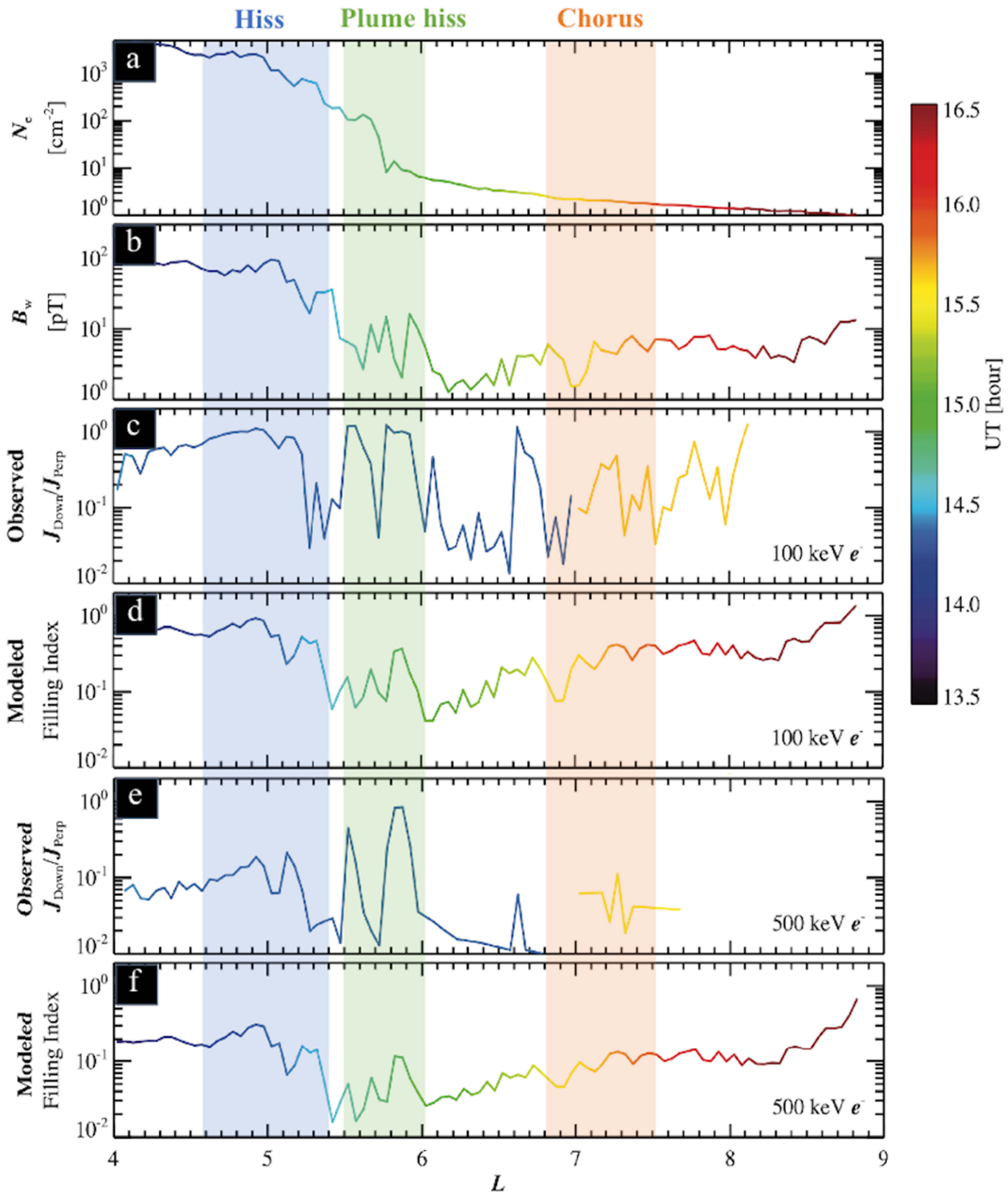

572

573 **Figure 4.** Comparison between the observed and the modeled electron precipitation over a large
574 *L* shell extent from 4 to 9 color-coded by UT. (a) Total electron density. (b) Whistler mode wave
575 magnetic amplitude. (c) Observed ratio of precipitating to trapped electrons at the 100 keV
576 energy channel. (d) Modeled ratio of precipitating to trapped electrons at the same energy as
577 shown in the panel (c). (e–f) Similar to panels (c–d) but for 500 keV electrons.

Figure 1.

Solar Wind and Geomagnetic Conditions

a

P_{dyn} [nPa]

5
4
3
2
1

B_z GSM [nT]

10
5
0
-5
-10

b

Sym-H [nT]

0
-10
-20
-30

AE [nT]

1000
100
10

UT
2020 Nov 27

1000
1200
1400
1600

ELFIN-A

c

E [keV]
Perp

10^3
10^2

10^9
10^8
10^7
10^6
Energy Flux [keV/(scm^{2}strMeV)]

d

E [keV]
Downward

10^3
10^2

10^9
10^8
10^7
10^6
Energy Flux

e

E [keV]
Down/Perp

10^3
10^2

10^0
10^{-1}
10^{-2}
Ratio

f

PA [°]
50-160 keV

180
90
0

Loss cone
Anti-loss cone

10^9
10^8
10^7
Energy Flux

g

PA [°]
160-345 keV

180
90
0

10^9
10^8
10^7
Energy Flux

h

PA [°]
345-900 keV

180
90
0

10^8
10^7
10^6
Energy Flux

i

PA [°]
>900 keV

180
90
0

10^7
10^6
10^5
Energy Flux

L	7.5	6.5	5.7	5.1	4.5
MLAT	-73.5	-71.6	-69.7	-67.8	-65.8
MLT	10.9	10.9	10.9	10.8	10.8
Seconds	30	00	30	00	30
2020 Nov 27	1422	1423		1424	

Figure 2.

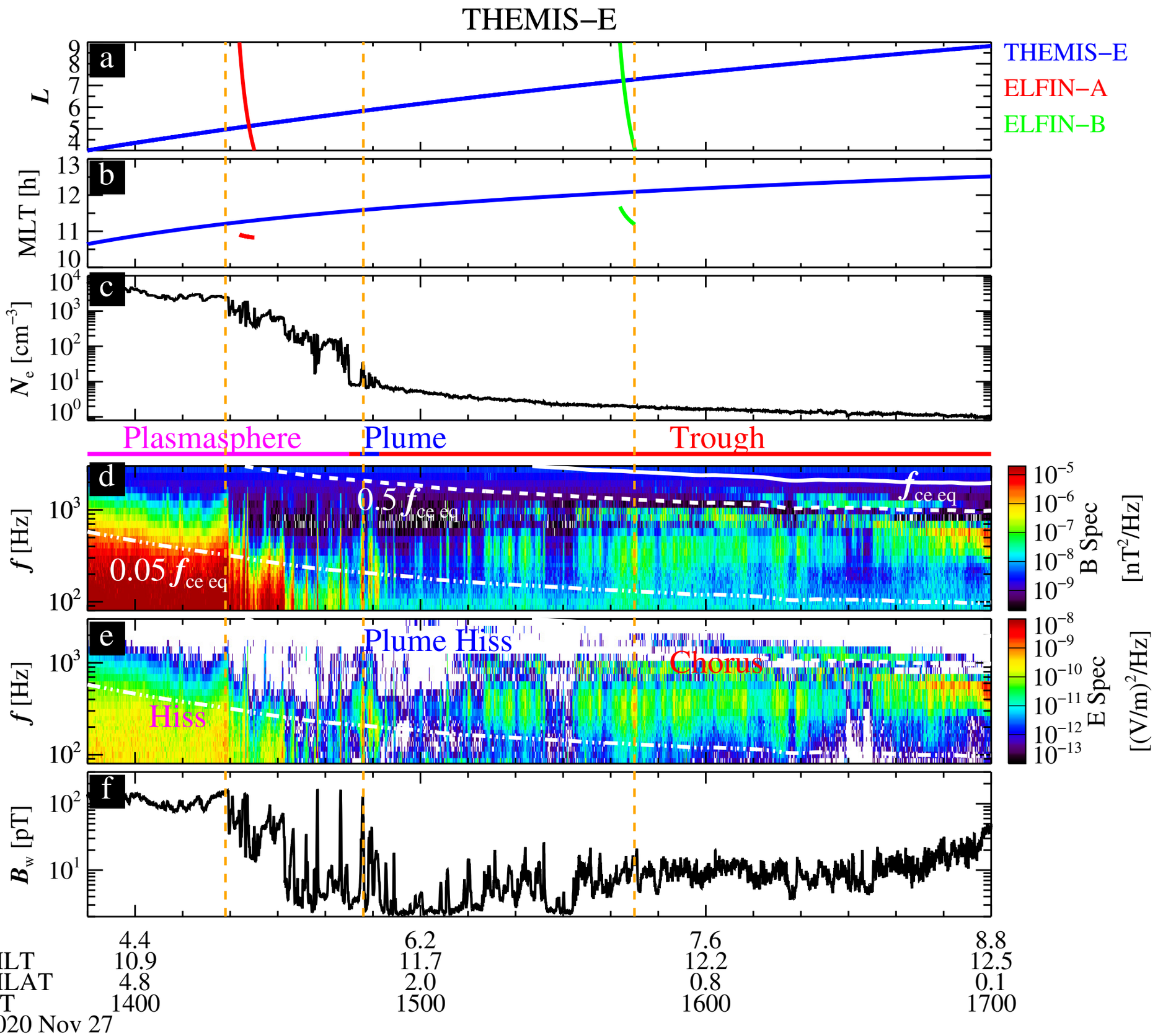
THEMIS–E
a
b
c
d
e
f
L
MLT [h]
N_e [cm^{-3}]
THEMIS–E
ELFIN–A
ELFIN–B
Plasmasphere
Plume
Trough
f [Hz]
0.5 $f_{ce\ eq}$
$f_{ce\ eq}$
0.05 $f_{ce\ eq}$
B Spec
[nT^2/Hz]
Plume Hiss
Chorus
Hiss
E Spec
[(V/m)^2/Hz]
B_w [pT]
L 4.4 6.2 7.6 8.8
MLT 10.9 11.7 12.2 12.5
MLAT 4.8 2.0 0.8 0.1
UT 1400 1500 1600 1700
2020 Nov 27

Figure 3.

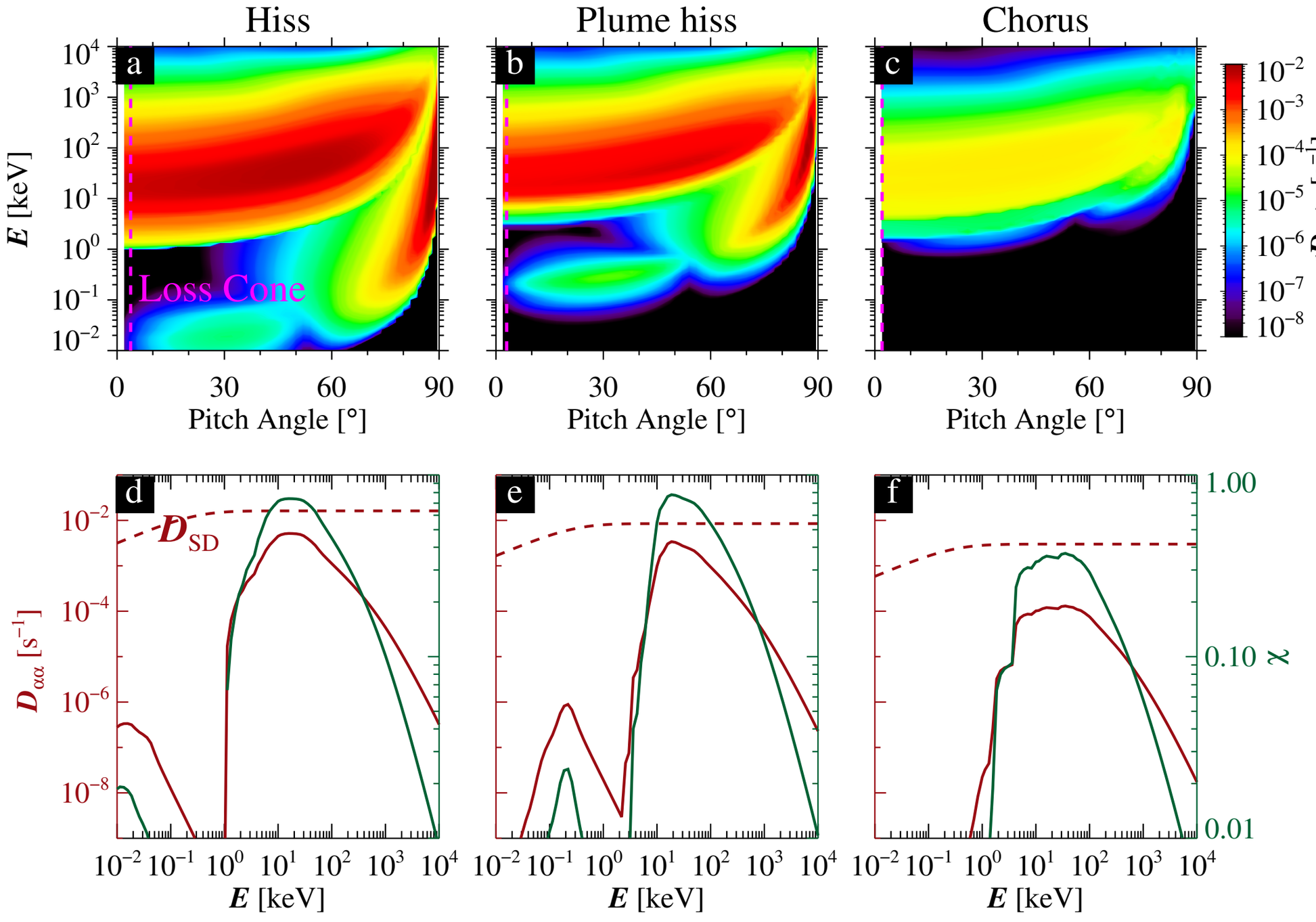
Hiss
Plume hiss
Chorus
a
b
c
Loss Cone
E [keV]
Pitch Angle [°]
<D_αα> [s^-1]
d
e
f
D_SD
D_αα [s^-1]
E [keV]
χ
1.00
0.10
0.01

Figure 4.

Hiss
Plume hiss
Chorus
a
N_e [cm^{-2}]
10^3
10^2
10^1
10^0
b
B_w [pT]
10^2
10^1
10^0
c
Observed
J_{Down}/J_{Perp}
10^0
10^{-1}
10^{-2}
100 keV e^-
d
Modeled
Filling Index
10^0
10^{-1}
10^{-2}
100 keV e^-
e
Observed
J_{Down}/J_{Perp}
10^0
10^{-1}
10^{-2}
500 keV e^-
f
Modeled
Filling Index
10^0
10^{-1}
10^{-2}
500 keV e^-
4
5
6
7
8
9
L
16.5
16.0
15.5
15.0
14.5
14.0
13.5
UT [hour]